aerospace

MDPI

Article

Ground Vibration Testing of a Flexible Wing: A Benchmark and Case Study

Gabriele Dessena [1,*], Dmitry I. Ignatyev [1], James F. Whidborne [1], Alessandro Pontillo [2] and Luca Zanotti Fragonara [1]

[1] School of Aerospace, Transport and Manufacturing, Cranfield University, Cranfield, Bedforshire MK43 0AL, UK
[2] Department of Aerospace Engineering, University of Bristol, Bristol BS8 1QU, UK
* Correspondence: gabriele.dessena@cranfield.ac.uk

Abstract: Beam-like flexible structures are of interest in many fields of engineering, particularly aeronautics, where wings are frequently modelled and represented as such. Experimental modal analysis is commonly used to characterise the wing's dynamical response. However, unlike other flexible structure applications, no benchmark problems involving high-aspect-ratio flexible wings have appeared in the open literature. To address this, this paper reports on ground vibration testing results for a flexible wing and its sub-assembly and parts. The experimental data can be used as a benchmark and are available to the aeronautical and structural dynamics community. Furthermore, non-linearities in the structure, where present, were detected. Tests were performed on the whole wing as well as parts and sub-assembly, providing four specimens. These were excited with random vibration at three different amplitudes from a shaker table. The modal properties of a very flexible high-aspect-ratio wing model, its sub-assembly and parts, were extracted, non-linear behaviour was detected and the experimental data are shared in an open repository.

Keywords: modal analysis; experimental modal analysis; flexible wing; ground vibration testing; beam vibration testing; shaker testing; dynamic testing; high aspect ratio; non-linear dynamics

Citation: Dessena, G.; Ignatyev, D.I.; Whidborne, J.F.; Pontillo, A.; Fragonara, L.Z. Ground Vibration Testing of a Flexible Wing: A Benchmark and Case Study. *Aerospace* **2022**, *9*, 438. https://doi.org/10.3390/aerospace9080438

Academic Editor: Hekmat Alighanbari

Received: 27 June 2022
Accepted: 7 August 2022
Published: 10 August 2022

1. Introduction

As aeronautical technology progressed over the last 70 years, an increasing use of lightweight and composite materials has allowed designers and manufacturers to create a new state of the art for aircraft design. The likes of Boeing 787 and Airbus A350 have a higher proportion of composite and lightweight structures than ever before, driven by the need for, more efficient, high-aspect-ratio (HAR) wings [1]. Nevertheless, this approach has its shortcomings, particularly concerning the prediction and modelling of such flexible structures. Hence, new tools and procedures are needed. To address these issues, projects such as the Beam Reduction and Dynamic Scaling (BeaRDS) framework [2–5] were carried out to help the development of the aircraft, particularly wings, of the future. However, the issue remains largely open not only from an industrial point of view, but also from the academic side. In fact, while it is trivial to find benchmarks and open datasets for structural health monitoring or seismic vibration, the same cannot be said for flexible wings. The authors propose closing this gap by introducing a case study, benchmark and datasets for a flexible wing. Hence, this work aims to (i) report on the Ground Vibration Testing (GVT) results for a flexible wing and its sub-assembly and parts, (ii) detect, if any, non-linearities in the structure and (iii) share the experimental data to be used as a benchmark by the aeronautical and structural dynamics community.

The specimens used in this work were developed within the BeaRDS framework and include the eXperimental BeaRDS-2 (XB-2) HAR wing, its sub-assembly and its parts. These were tested with a random vibration at three different amplitudes, the data were post-processed and the modal parameters were extracted via Least Squares Complex Exponential

(LSCE) [6,7] from the systems' Frequency Response Functions (FRFs). The modal parameters and the near resonance FRF region were also used for the detection of non-linear behaviour. In addition, the experimental data were shared in an open repository and can be accessed via the Data Availability Statement.

Structural integrity is of paramount importance in engineering, and the knowledge and control of the vibrations of a system is a common part of the design of many products, such as fuel pumps [8] and suspended bridges [9]. For these objectives, refined Finite Element Models (FEMs) and experimental testing were carried out. In particular, *linear* Experimental Modal Analysis (EMA) was used to obtain the structure's modal parameters, such as natural frequencies (ω_n), damping ratios (ζ_n) and mode shapes ($\boldsymbol{\phi}_n$) [10]. These data are used for various applications, such as damage detection [11] and model updating [12].

In aeronautics, the term GVT is preferred over EMA. GVT is a rather standard procedure in the final stages of an aircraft project development and certification [13], and can also be used to detect inconsistencies in the building processes and materials used [14].

GVT is usually undertaken on entire craft, such as fighter jets [15], civil airliners [16] and unmanned aerial vehicles [17], or parts of them, such as helicopter blades [18]. The main objective of these procedures in aeronautics is the extraction of modal parameters used to update FEMs [19], rather than for damage detection. The usual procedure is to couple the FEM with an aerodynamic model to obtain the aeroelastic behaviour [20]. In order to obtain good correlation between the FEM and the real structure, the FEM needs to be tuned according to the results obtained via GVT, ensuring the final concept is compliant with the aeroelastic properties and dynamical response obtained from FEMs [21].

Damage detection would be impractical, as GVTs are usually lengthy and costly procedures performed in experimental settings on the ground. Nevertheless, it is still important to assess the state of a system [22]. This can be achieved with Operational Modal Analysis (OMA) [23]. OMA allows for the collection of experimental data during the operational life of a structure and allows us to obtain modal parameters [24] that can be either used for direct or model-based damage assessment. In particular, such model-based approaches can be used not only to obtain information about the health of the structure, but also of its new dynamics, such as aeroelastic onset speeds [25]. However, any OMA application is not considered here because GVT is the scope of this work.

In *linear* EMA, three main excitation techniques are usually used: sweep sine, random vibration and impulse testing. Each of them has advantages and disadvantages, which are beyond the scope of this paper; the reader can consult [26,27] for a deeper insight. As this work deals with a flexible wing, structural non-linearities should also be considered. In the last 30 years, major advances have been made in the development of *Non-linear* Modal Analysis (NLMA), which can be described as a three-step procedure [28]: detection, (ii) characterisation and (iii) parameter estimation. This work focuses only on the first of the three steps. Both sine sweep [29] and random vibration [30] have been used to detect non-linearities. Since non-linearity in sine sweep approaches is detected via distortions in the FRF [27] and these distortions can also depend on the sweep rate (e.g., too fast) [26], random vibration is selected as the chosen input for this work. The trend, and difference in modal parameters, predominantly ω_n, and the near resonance regions of the FRFs of the experiments at different input amplitudes are used to detect non-linearities, as proposed in [27]. The reader interested in a more in-depth review of NLMA and non-linear dynamics in general is referred to the classical reviews [28,31] and the book [27], while for practical applications, the following works are suggested [15,32,33].

Modal parameters identification was carried out with a single method, as it is customary for vibration testing campaigns [34], and because it was shown, for a related structure [24], that the modal parameters are independent of the technique used. The method selected is a frequency domain implementation of the industry standard method LSCE [35]. LSCE was introduced to overcome, acquiring single-input multiple-output capability, the single-input single-output limitations of the Complex Exponential Method [6,7]. The LSCE method requires, as a starting point, the Impulse Response Func-

tions (IRFs) of the system, which are then fitted with a set of complex damped sinusoids via Prony's method [36,37]. This allows the poles of the systems and the modal parameters to be found. In this implementation, the IRF is computed via inverse Fourier transform from the FRF. The LSCE implementation used in this work was adapted from MATLAB's function `modalfit` to be used in conjunction with an in-house-developed stabilisation diagram routine.

The remainder of this article is organised as follows. In Section 2 the specimens used within this work are outlined, a set of numerical and theoretical predictions is given, then the test set-up is described and, finally, the data processing and the identification procedure are shown. Section 3 presents the results obtained, Section 4 discusses the results and Section 5 presents the conclusions and closing remarks.

2. Materials and Methods

This section is concerned with the description of the specimens and the context behind their design and manufacture. Theoretical and numerical predictions, alongside data from a previous testing campaign, are presented as a source for comparison. The experimental set-up is shown and, finally, the data processing and the parameters identification strategy are outlined.

2.1. The XB-2 High Aspect Ratio Wing

The XB-2 HAR wing was designed under the BeaRDS framework, Figure 1, a project developed within Cranfield University which aimed to establish a process for the design, manufacture and testing of dynamically scaled HAR wings for use in Cranfield University's 8′ × 6′ wind tunnel. The XB-2 was a scaled down version of an optimised full-scale wing designed to minimise induced drag on an A320-like aircraft [4], which was scaled down for wind tunnel testing [3]. The wing consists of four main components: the main spar, the stiffening tube (or the tube), the additional brass masses for the purpose of dynamic scale parameters matching (or the masses) and the skin. However, for the purpose of this study, the masses are removed.

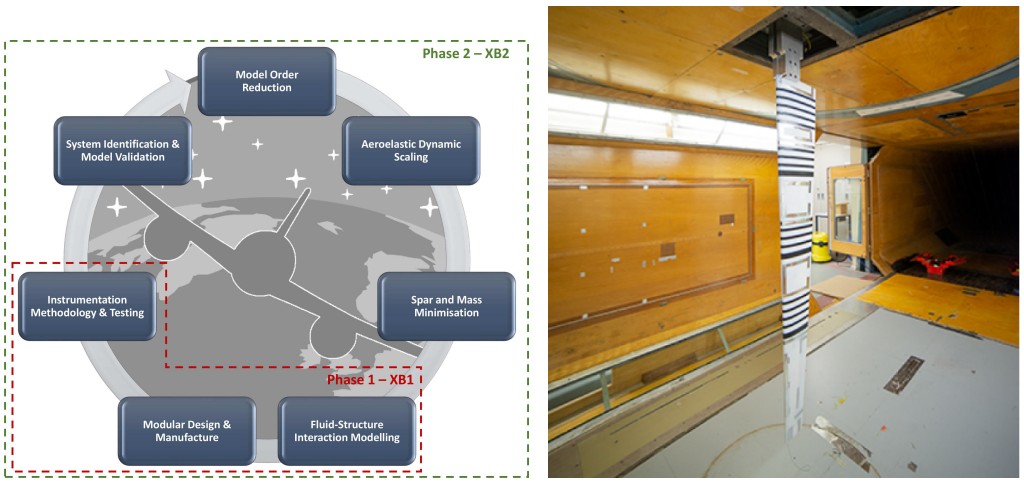

(**a**) (**b**)

Figure 1. (**a**) BeaRDS work flow (Retrieved from [2]) and (**b**) XB-2 in the 8′ × 6′ Cranfield University's wind tunnel (Retrieved from [5]).

The XB-2 spar is made of 6082-T6 Aluminium. The tube and the connections are made of Stainless Steel, and the skin is made of strips of 3D printed Digital-ABS [38] and Agilus 30 [39], a rubber-like material printed together to guarantee the structural continuity of the wing skin (no gaps). Figure 2 shows the skin's Digital-ABS and Agilus 30 sections, respectively, in white and black. The bespoke skin constitutes the aerodynamic surface of the wing, which is outlined by a NACA 23015 aerofoil and spans for 1.5 m. The mean

aerodynamic chord is 0.017 m with a taper ratio of 0.35, a Leading Edge sweep (Λ_{LE}) of 1.49° and a sweep $c/4$ ($\Lambda_{c/4}$) of 0°. The wing does not feature any dihedral or twist. The materials and physical properties are presented in Table 1. The subsequent subsection introduces XB-2 wing's parts in detail.

Figure 2. XB-2 wing top view.

Table 1. Materials and physical properties.

Property	Details	Unit	Material	Young Modulus [GPa]	Poisson Ratio [-]	Density [kgm^{-3}]
Semi span	1.5	m	6082-T6 Aluminium	70	0.33	2700
$\bar{c}$	172	mm	Stainless Steel	193	0.33	8000
midrule λ	0.35	-	Digital ABS	2.6–3.0	0.33 [14]	1170–1180
Λ_{LE}	14.9	°	Agilus 30	NA	NA	1140
$\Lambda_{c/4}$	0	°				
Aerofoil	NACA 23015	-				
Mass	3.024	kg				

2.1.1. The Spars

The spar is made of 6082-T6 Aluminium Alloy, and it can be divided into three sections according to its span-wise position and geometric characteristics: root, mid-span and tip.

As shown in Figure 3, the spar features a Saint George's cross-shaped cross section, which changes proportions along the span, and a rectangular cross section in the root section, where the spar can be clamped. The three locations of interest along the span (root, mid-span and tip) are given in Table 2, where positions are with respect to the centroid of the root section's extremity: X-axis is in span-wise direction and positive in the outward direction, Y-axis describes the vertical placement with the positive direction upwards and the Z-axis is the depth, positive in the LE to TE (Trailing Edge) direction, as shown in Figure 3. Due to a manufacturing constraint, the spar was machined from two separate aluminium blocks, which were welded at mid-span and secured by a bolted bridge plate.

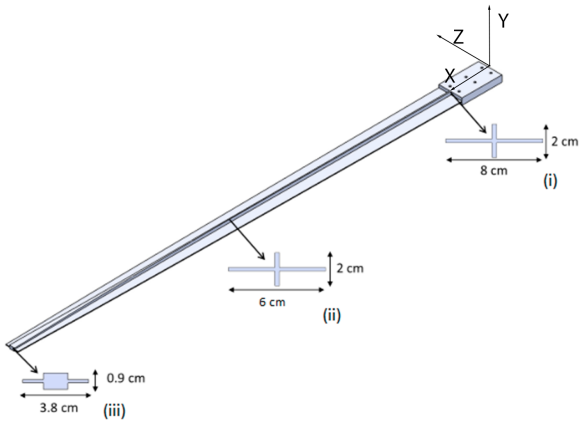

Figure 3. Main spar CAD model with section view at the location of interest: (**i**) root, (**ii**) mid-span, and (**iii**) tip (adapted from [3]).

Table 2. Spar's interest points location.

Section	X [m]	Y [m]	Z [m]
Root	0.125	0	0
Mid-span	0.875	0	0
Tip	1.45	0	0

Two identical samples of the spar specimen were manufactured, which we will refer to as the main spar and the twin spar for the remainder of the article. The twin spar was used for ground testing within BearDS, while the main spar is the specimen that served as the spar of the model tested in the wind tunnel. Their main difference is in the way the two halves are joined. The main spar features a reinforced bridge plate, featuring a "L" profile, rather than the simple plate used for the twin spar, as shown in Figure 4.

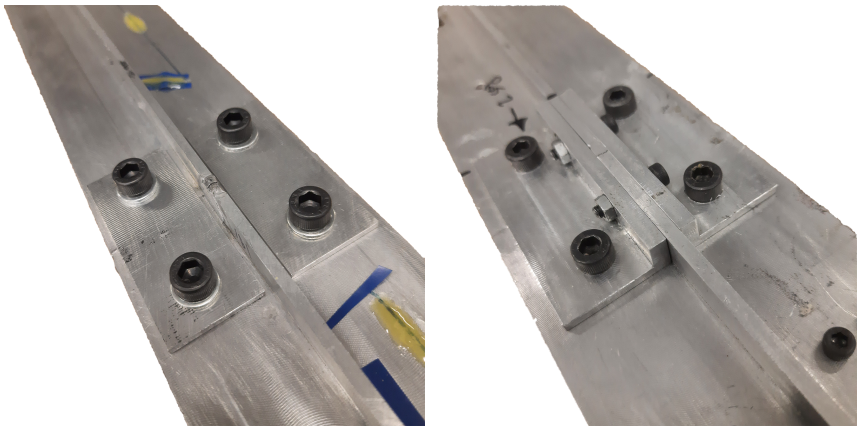

(**a**) (**b**)

Figure 4. (**a**) Shows the reinforced plate of the twin spar, while (**b**) shows the bridge of the main spar.

Another difference emerged when XB-2 was disassembled; the main spar was plastically deformed near the root, resulting in a 55 mm vertical deviation at the tip. The twin spar weights 1.220 kg and the main spar 1.225 kg. Table 3 remarks on the differences between the twin and main spar.

Table 3. Specimens of the testing campaign.

Specimen	Description	Mass [kg]
Twin spar	The twin spar is a spar that was manufactured for ground testing only and it is recognisable from the main, or actual, spar for its bridge plate, as shown in Figure 4a.	1.220
Main spar	This is the spar used for the wind tunnel testing of XB-2 and its recognisable from the twin spar for its deformed shape and L profiled bridge plate, Figure 4b.	1.225

2.1.2. The Tube

The tube was introduced in the original scaling process of the full-scale wing to stiffen the wing sub-scale model and prevent flutter onset during wind tunnel testing [3]. It is placed parallel to the main spar, and it is attached to it at three points, as shown in Figure 5. The tube and links are made of Stainless Steel. The tube has an outer diameter of 10 mm and a thickness of 1 mm. The three rigid links and the tube's ends are positioned as per Table 4, where the reference is the same as considered for Table 2. The tube weighs 0.130 kg, and after its assembly with the main spar, shown in Figure 5, it weighs 1.362 kg.

Figure 5. The spar and tube assembly.

Table 4. Spar's interest points location.

Section	X [m]	Y [m]	Z [m]
Tube inner end	0.157	−0.002	0.045
First link	0.170	0	0.045
Second link	0.430	0	0.045
Third link	0.690	0	0.045
Tube outer end	0.707	−0.002	0.045

2.1.3. The Skin

The wing's skin is divided into four sections made up of 47 different subsections, which were 3D printed in Digital ABS and Agilus 30. The skin provides the aerodynamic shape to the wing and transfers the aerodynamic loads to the underlying structure. As shown in Figures 1b and 2, the black stripes on the wing are the rubber-like Agilus 30 strips, while the rest of the skin is made of Digital ABS. Remarkably, each section is printed using the two different materials within the same print by using the Polyjet technique and not requiring gluing, or any other form of assembly, between the different stripes. With this arrangement in mind, the Agilus 30 stripes allow the skin to be flexible without compromising its integrity. The full wing assembly, as shown in Figure 2, weighs 3.024 kg.

2.2. Theoretical and Numerical Predictions

Prior to testing, a theoretical and a numerical prediction of the first three bending modes was performed. The numerical prediction was achieved via the Euler–Bernoulli beam theory by calculating the first three theoretical bending frequencies of the main spar, as per the following Equation [40]:

$$f_i = \frac{\lambda_i^2}{2\pi \mathrm{L}^2}\sqrt{\frac{\mathrm{EI}}{m}} \qquad i = 1,2,3$$
$$\text{for } \lambda_{1-3} = \{1.87510407, 4.69409113, 7.85475744\} \tag{1}$$

where λ is the natural frequency parameter, L is the beam length, E is the Young Modulus, I is the second moment of inertia of the beam section, averaged over the beam span, and m is the mass per unit length. The value of λ corresponding to the mode of interest can be found in Equation (1). The value of L corresponds to the beam's span outboard of the clamp, so it is 1.325 m, and likewise for m. The mass of the beam without the root section was estimated to be 650 g, and was divided by L to obtain m.

The numerical prediction was carried out with a FEM of the main spar, with the aim of identifying the first three bending modes' natural frequencies. The main spar was modelled as a tapered beam, with elements BEAM188 in ANSYS Mechanical APDL and the bridge at mid span as a lumped mass of 44 g. As a further source of comparison, the results of a previous GVT campaign [3] on the twin spar are reported. Nevertheless, the testing setup was different because the previous campaign used a stinger shaker, rather than a shaker table, which influences the identified results. In fact, it was found in [41], on a similar structure, that the ω_n identified from a stinger shaker were higher than those from a shaker table experiment, due to the interaction between the structure and the stinger. Table 5 shows the first three bending modes' natural frequencies of the twin spar from predictions and the previous testing campaign of the the twin spar [3].

Table 5. Results of the spar's natural frequencies' prediction and previous testing campaign.

Bending Mode	Theoretical	Numerical	GVT [3]
1st	5.166	5.183	5.27
2nd	32.373	30.837	27.12
3rd	90.646	106.060	83.39

2.3. Experimental Setup

A random verification for each input scenario was carried out for the twin spar, main spar, main spar and tube and full configuration of XB-2, as outlined in Table 6.

Table 6. Specimens of the testing campaign.

Specimen	Description	Mass [kg]
Twin spar	The twin spar is a spar that was manufactured for ground testing only, and it is recognisable from the main, or actual, spar for its bridge plate, as shown in Figure 4a.	1.220
Main spar	This is the spar used for the wind tunnel testing of XB-2 (Figure 4b).	1.225
Spar and tube	The spar and tube is the torque box of XB-2, which includes the main spar and the tube (Figure 5).	1.362
Full wing	This is the XB-2 wing, comprising spar, tube and skin (Figure 2).	3.024

The specimens were driven by a Data Physics® Signal Force™ modal shaker controlled by DP760™ closed-loop control software running on a consumer-grade laptop. The data were collected by nine accelerometers, as per Table 7, and positioned along the span, as per Figure 6. One further accelerometer was placed on the clamp, serving as feedback for the shaker. The accelerometers are connected to a National Instruments cDAQ-9178, saving the data on a desktop machine via a LabVIEW program developed in-house. The experimental setup schematic is found in Figure 7. The accelerometer's span-wise position was decided using a sensor placement routine based on a genetic algorithm [42]. The FEM model used for the theoretical predictions was employed as a baseline, and a genetic algorithm minimised the sum of the off-diagonal terms of the autoMAC (Modal Assurance Criterion between the modes themselves) by varying the sensors position along the span.

Table 7. Accelerometers specifications.

ID #	Accelerometers Model	Sensitivity [mVg^{-1}]	Mass [g]
0	PCB Piezotronics® model: 352C23	4.88	0.2
1R	PCB Piezotronics® model: 356A16	96.5	7.4
1L	Isotron® accelerometer model 7251A	10.3	10.5
2R	PCB Piezotronics® model: 356A16	97.2	7.4
2L	Isotron® accelerometer model 7251A	10.08	10.5
3R	PCB Piezotronics® model: 356A45	100.2	4.2
3L	Isotron® accelerometer model 7251A	10.34	10.5
4R	Brüel & Kjær® accelerometer type 4507-002	94.12	4.8
4L	Brüel & Kjær® accelerometer type 4507-002	95.52	4.8

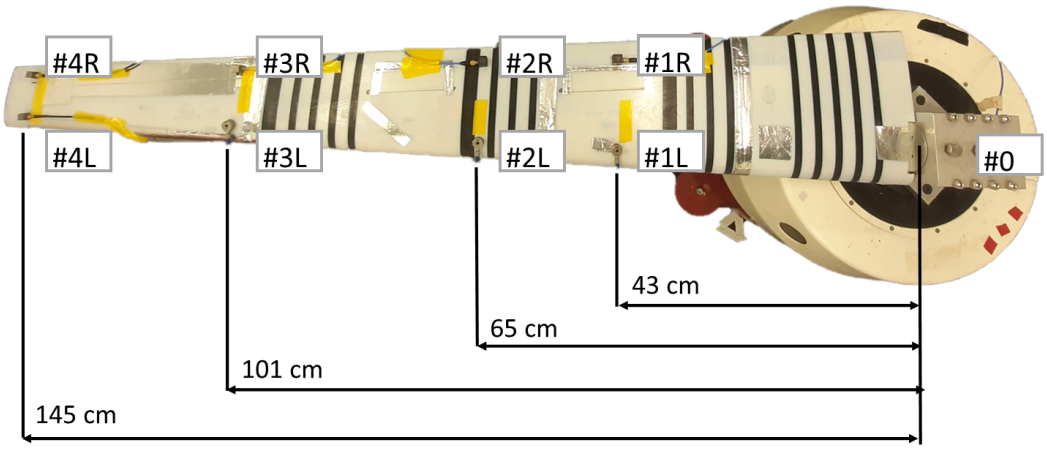

Figure 6. Accelerometers locations. The accelerometers do not appear aligned only for the optical effect of the camera lens.

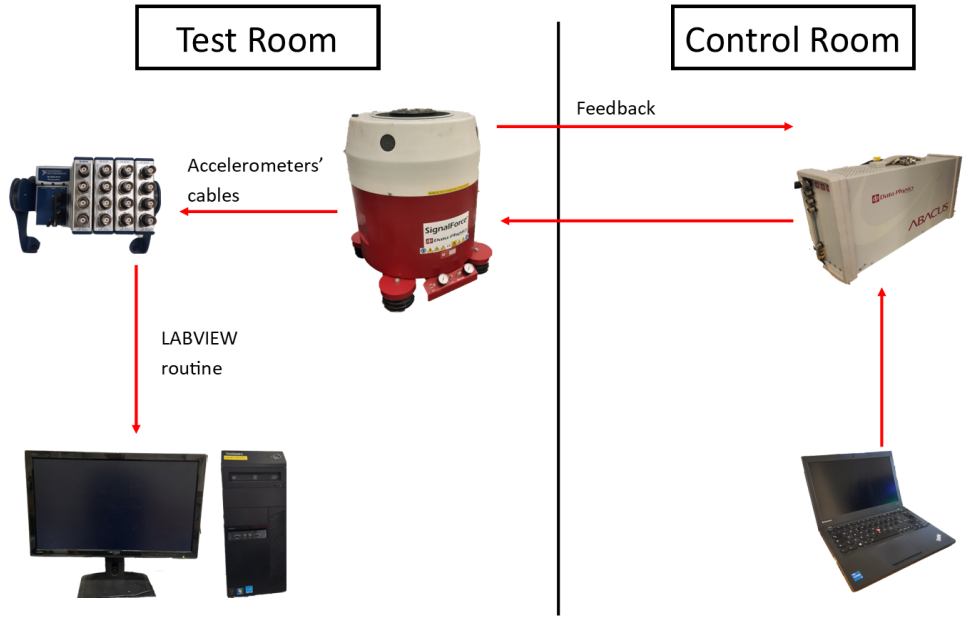

Figure 7. Testing setup.

A random verification of different amplitude was used. A low, medium and high input level corresponded, respectively, to 0.305, 1.034 and 1.712 g RMS values. These input scenarios are referred to, respectively, as the low-, medium- and high-input scenario for the remainder of this article. The random input signal was bandwidth limited between 2 and 400 Hz and had a 20 min duration.

2.4. Data Processing and Identification

Accounting for transients and consistency, the signals in the accompanying data [43] lasted 18 min, instead of 20, with a sampling frequency (f_s) of 256 Hz, down-sampled from the original $f_s = 5120$ Hz to smooth out the signal. Only the results for single realisation of each scenario for each specimen are reported in this study, as the length of the signal and the nature of the input mitigate any possible significant discrepancies with repeated measurements. Since accelerometers #1-3R were tri-axial, the horizontal (Z-axis as per Figure 3) accelerations were recorded at those positions. Nevertheless, these analyses focus on the vertical and torsional modes of the specimens; hence, those data were disregarded for identification. Given the three input amplitudes and the four specimens,

twelve different testing cases exist, for which the first three modes' modal parameters, where vertical displacement was dominant, were extracted.

The signal, originally in g, was converted to ms^{-2} for adherence with the SI units, and band limited between 2.5 and 98 Hz to exclude the drifts at high and low frequency. The FRFs were computed in the usual fashion, by element-wise division of the output's FFT with the input's FFT, with channel #0 as the input. A Savitzky–Golay filter of order 3 and length 601 was then applied to smooth out the response. At this point, the LSCE method was employed within a stabilisation diagram to identify the physical modes of all cases. The identification order ranged from 3 to 32 with steps of unity, and the stable modes were identified using the relative frequency (Δf) and damping ($\Delta\zeta$) and the MAC (Modal Assurance Criterion) of order-wise adjacent modes. The results of this procedure are presented in the following section.

3. Results

This section introduces the results obtained from the process outlined in the previous section. The results are presented separately for each specimen and input amplitude scenario. The data are presented both visually and numerically, presenting the FRFs computed from the experiment, the stabilisation diagram, a table with the identified modal parameters, the mode shapes diagrams and the FRFs' resonances comparisons.

3.1. Twin Spar

Figure 8 shows the magnitude and phase for the FRFs of the high- and low-input scenarios. The first three resonance frequencies are clearly visible in both the magnitude and phase plot, where they are identified by, respectively, the peaks and phase change. The stabilisation diagram for the low-input scenario is shown in Figure 9. The identified ω_n and ζ_n for the three input cases are reported in Table 8 for the first three modes identified, which are all bending modes. Additionally, Table A1 reports the raw identification data. Figure 10 compares the first three identified mode shapes for the three-input scenario with the baseline shape. The three $\boldsymbol{\phi}_{1-3}$ are pure bending modes and feature the expected shape from theory. Lastly for the twin spar, Figure 11 compares the FRF magnitude of the outermost left channel near the first three resonances.

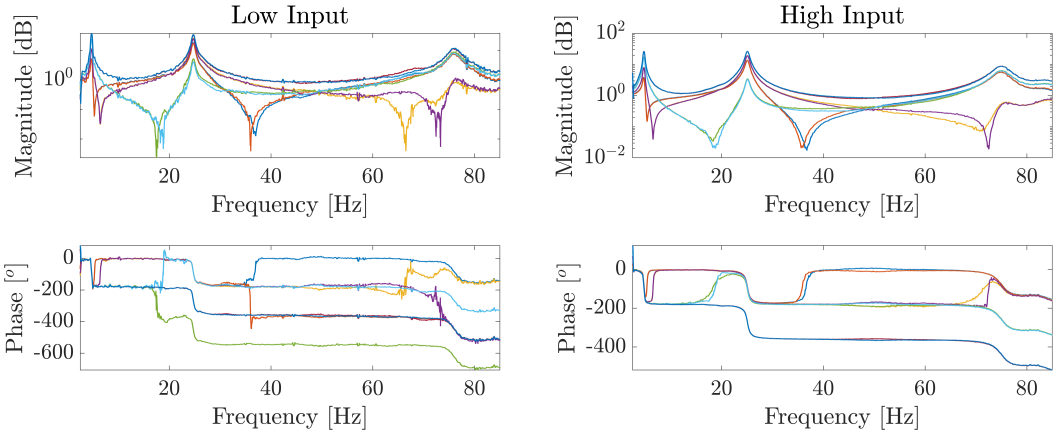

Figure 8. Twin spar: FRFs of the low and high input scenarios. All channels are superimposed for conciseness.

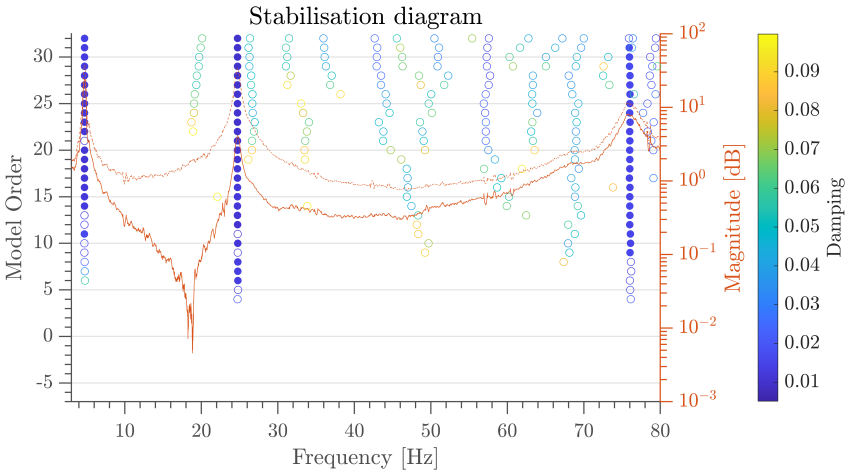

Figure 9. Twin spar: stabilisation diagram of the low-input scenario computed with the following parameters: $\Delta f = 1\%$, $\Delta\zeta = 5\%$ and MAC $= 0.95$. The FRF of channels # 3L and 4L are superimposed for further mode visualisation.

Table 8. Twin spar: Natural frequency and damping ratio parameters.

Bending Mode	Input: Low		Medium		High	
	ω_n [Hz]	ζ_n [-]	ω_n [Hz]	ζ_n [-]	ω_n [Hz]	ζ_n [-]
1st	4.731	0.013	4.742	0.027	4.738	0.029
2nd	24.732	0.010	25.021	0.021	25.087	0.016
3rd	75.939	0.017	75.124	0.021	75.016	0.022

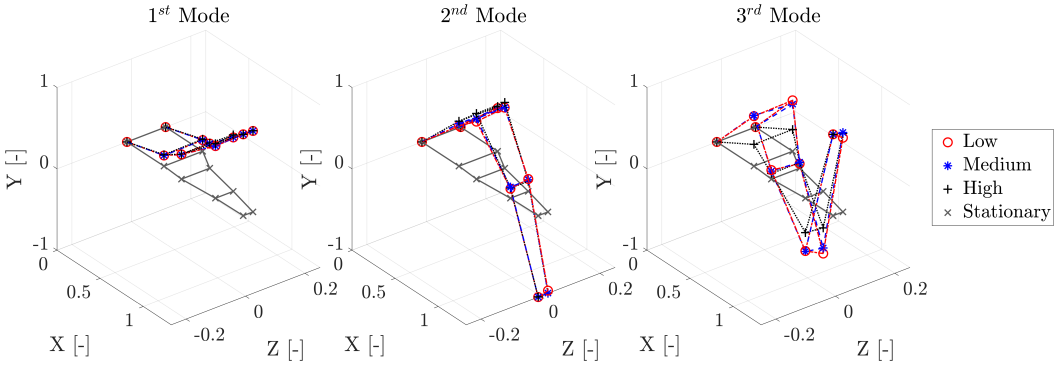

Figure 10. Twin spar: mode shapes of the first three vertically dominant modes.

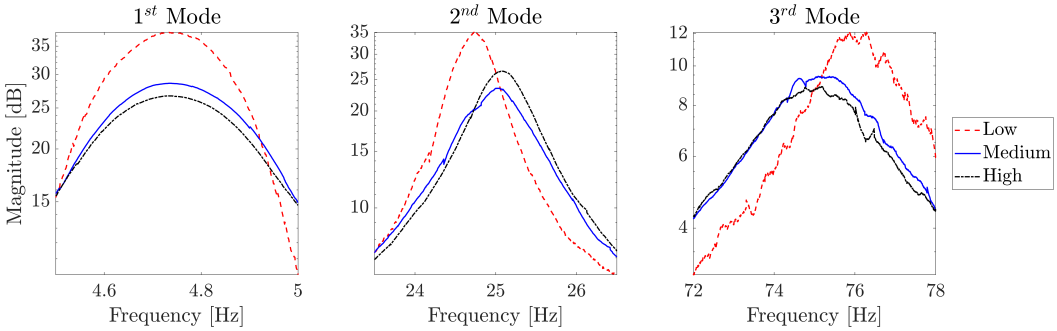

Figure 11. Twin spar: comparison of the FRFs of channel #4L for the three input scenarios near resonances.

The following subsections' content is presented in the same manner, and remarks are made only when necessary or when results need further insight.

3.2. Main Spar

As per Section 3.1, the FRFs of the low-, medium-, and high-input scenarios are presented in Figures 12 and 13 shows the stabilisation diagram for the low input case, while Table 9 presents the identified natural frequencies and damping ratios and Figure 14 displays the comparison between the mode shapes of the two input cases. Finally, Figure 15 compares the near-resonance region of the FRFs computed from channel #4L for the three input scenarios. The raw identification data are reported in Table A2.

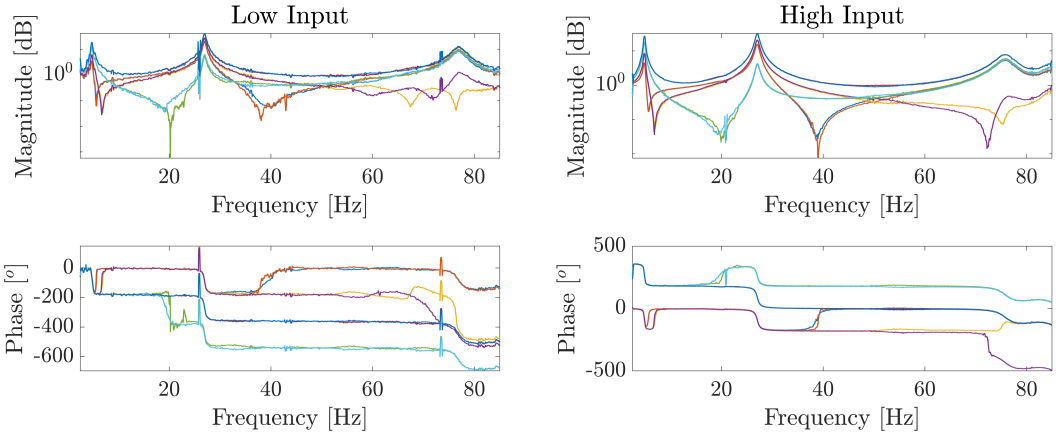

Figure 12. Main spar: FRFs of the low- and high-input scenarios. All channels are superimposed for conciseness.

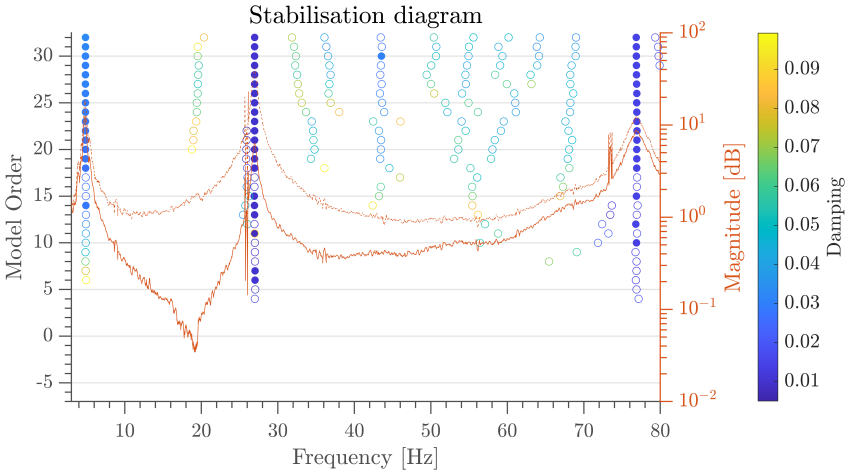

Figure 13. Main spar: Stabilisation diagrams showing the low-input scenario computed with the following parameters: $\Delta f = 1\%$, $\Delta\zeta = 5\%$ and MAC $= 0.95$. The FRF of channels # 3L and 4L are superimposed for further mode visualisation.

Table 9. Main Spar: natural frequency and damping ratio parameters.

Bending Mode	**Input**					
	Low		**Medium**		**High**	
	ω_n **[Hz]**	ζ_n **[-]**	ω_n **[Hz]**	ζ_n **[-]**	ω_n **[Hz]**	ζ_n **[-]**
1st	4.855	0.033	4.866	0.029	4.876	0.029
2nd	26.966	0.010	27.050	0.016	27.057	0.014
3rd	76.851	0.014	76.195	0.020	75.805	0.022

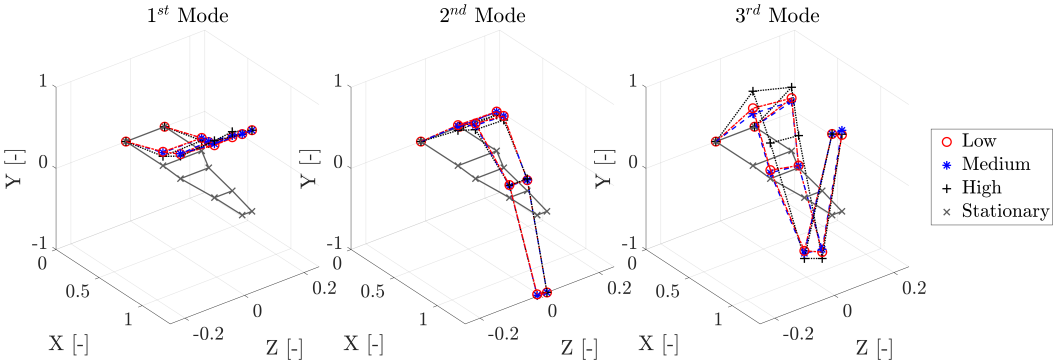

Figure 14. Main spar: mode shapes of the first three vertically dominant modes.

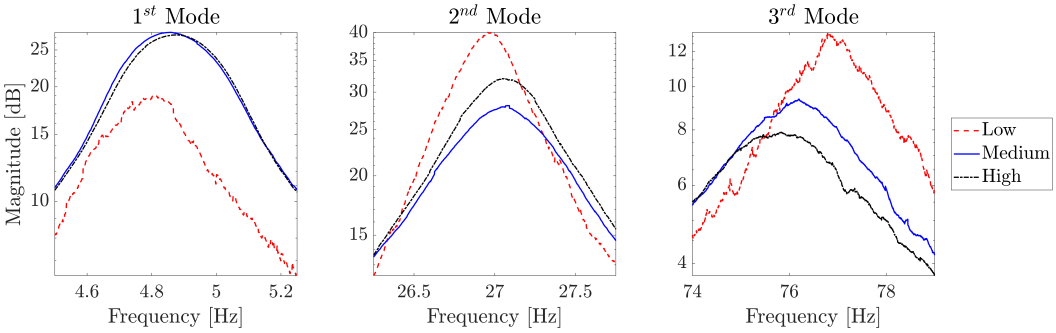

Figure 15. Main spar: comparison of the FRFs of channel #4L for the two input scenarios near resonances.

3.3. Spar and Tube

The spar and tube results are reported in the same fashion as in Sections 3.1 and 3.2. Figure 16 shows the superimposed FRFs channels, Figure 17 shows the stabilisation diagrams for the low- and high-input scenarios, Table 10 reports the identified natural frequencies and damping ratios, Figure 18 shows the first three vertical dominant modes and, finally, Figure 19 shows the comparison of the FRFs of the outermost left channel. In Table A3, the raw identification data are reported.

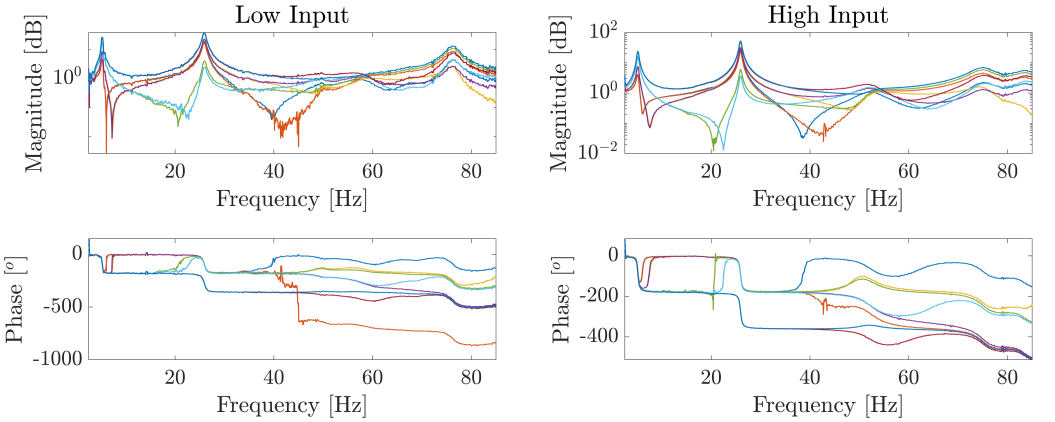

Figure 16. Spar and tube: FRFs of the low- and high-input scenarios. All channels are superimposed for conciseness.

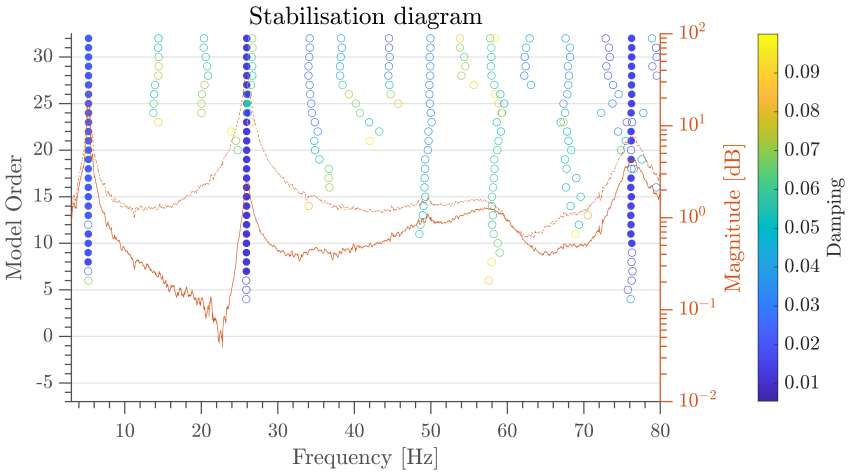

Figure 17. Spar and tube: Stabilisation diagrams the low-input scenario computed with the following parameters: $\Delta f = 1\%$, $\Delta\zeta = 5\%$ and MAC $= 0.95$. The FRF of channels # 3L and 4L are superimposed for further mode visualisation.

Table 10. Spar and tube: Natural frequency and damping ratio parameters.

Bending Mode	**Input**					
	Low		**Medium**		**High**	
	ω_n **[Hz]**	ζ_n **[-]**	ω_n **[Hz]**	ζ_n **[-]**	ω_n **[Hz]**	ζ_n **[-]**
1st Bending	5.252	0.022	5.151	0.030	5.163	0.036
2nd Bending	25.933	0.014	25.958	0.011	25.941	.010
3rd Coupled	76.242	0.017	75.770	0.034	75.135	0.034

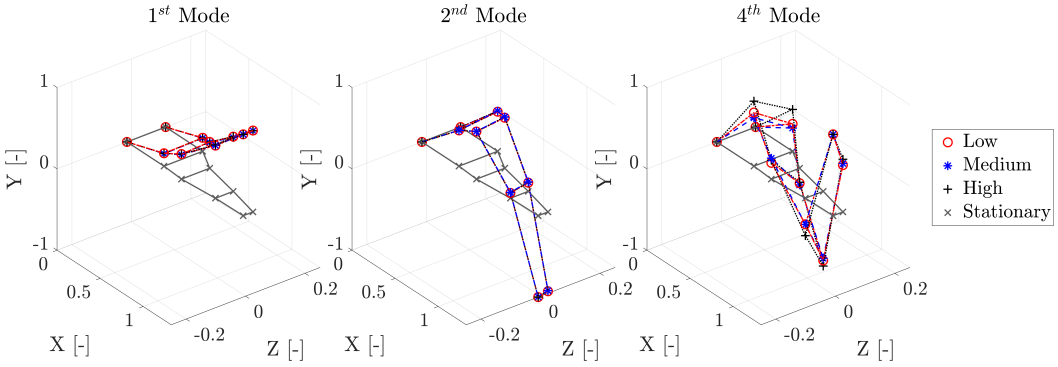

Figure 18. Spar and tube: Mode shapes of the first three vertically dominant modes.

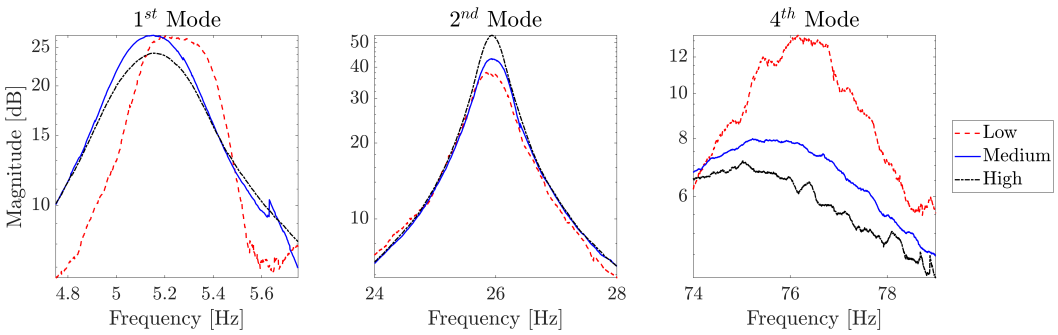

Figure 19. Spar and tube: Comparison of the FRFs of channel #4L for the two input scenarios near resonances.

3.4. Full Wing

The results for the full wing are reported in the same fashion as in previous sections. Figures 20 and 21 show the FRFs, superimposed for conciseness, of the low- and high-input scenario, Table 11 reports the identified natural frequencies and damping ratios, Figures 22 and 23 show the identified $\boldsymbol{\phi}_{1-2,4}$. Table A4 shows the raw identification data.

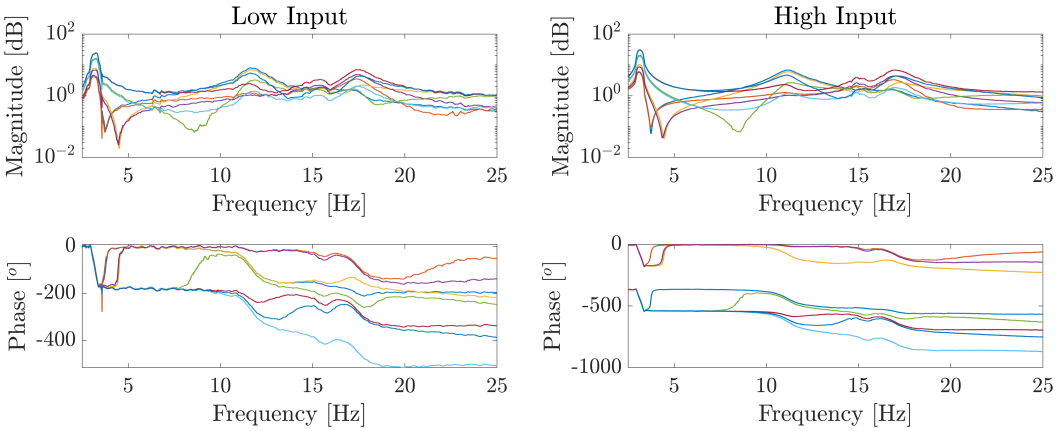

Figure 20. Full Wing: FRFs of the low- and high-input scenarios. All channels are superimposed for conciseness.

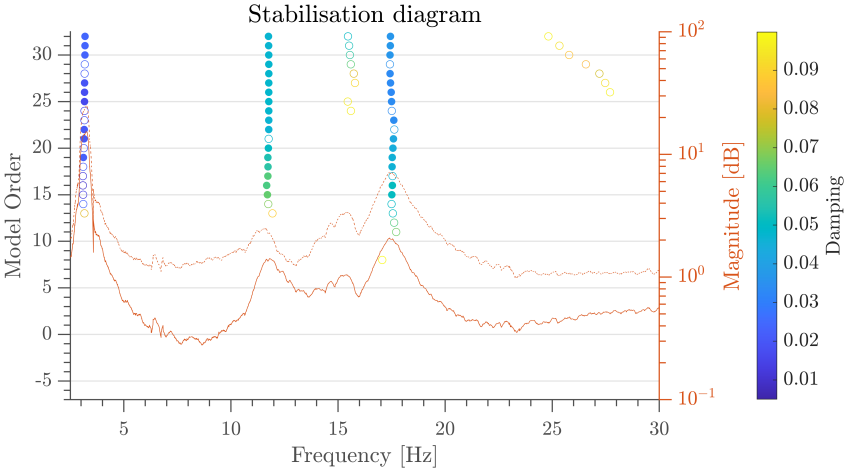

Figure 21. Full wing: stabilisation diagrams the low-input scenario computed with the following parameters: $\Delta f = 1\%$, $\Delta\zeta = 5\%$ and MAC $= 0.95$. The FRF of channels #3L and #4L are superimposed for further mode visualisation.

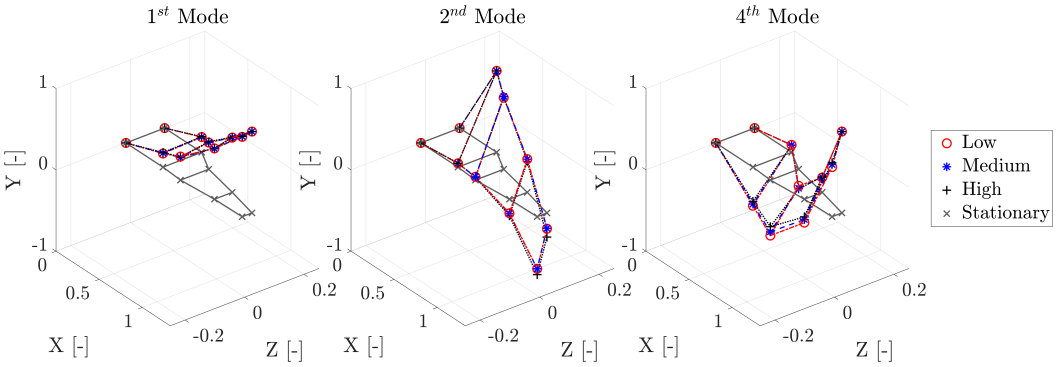

Figure 22. Full wing: mode shapes of the first three vertically dominant modes.

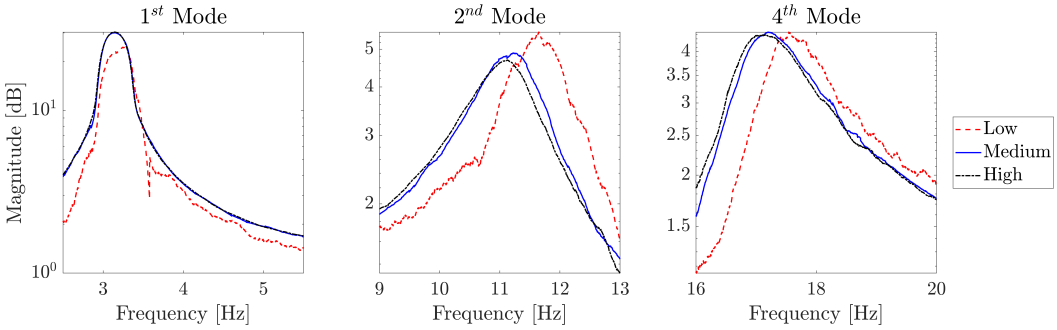

Figure 23. Full wing: comparison of the FRFs of channel #4L for the two input scenarios near resonances.

Table 11. Full wing: natural frequency and damping ratio parameters.

Bending Mode	Input					
	Low		Medium		High	
	ω_n [Hz]	ζ_n [-]	ω_n [Hz]	ζ_n [-]	ω_n [Hz]	ζ_n [-]
1st Bending	3.187	0.024	3.164	0.018	3.139	0.018
2nd Coupled	11.752	0.047	11.267	0.060	11.196	0.065
4th Coupled	17.447	0.037	17.070	0.041	16.988	0.042

4. Discussion

This section deals with the discussion of the results introduced in the previous section and is organised as follows: the discussion is carried out separately for each part or sub-assembly.

4.1. Twin Spar

The twin spar results are coherent with the previous campaign results and predictions. The data in Table 5 are used as a source of comparison with the theoretical, numerical predictions and previous testing for the identified data in Figure 1 and Table 8. Nevertheless, a small difference can be identified, but it should be noted that the previous testing campaign used a stinger shaker, rather than a shaker table, hence influencing the identified modal parameters. However, as expected from [41], the ω_n identified in this test are lower than those from [3]. It should be noted that $\boldsymbol{\phi}_3$, while conserving the overall shape, deviates from the trajectory of the same mode shape for lower amplitudes. The comparison within the three input scenarios shows that the modal parameters are influenced by the input strength. However, a clear overall relationship cannot be assessed. The variations are mostly evident for the second and third mode, for which, respectively, hardening and softening behaviour are observed. Nonetheless, the same does not hold for ζ_{1-3} and $\boldsymbol{\phi}_{1-2}$. From the results in Table 8 and Figure 10, the damping is not dependent on the input scenario and likewise for the mode shapes.

4.2. Main Spar

The main spar's modal parameters estimation is closely comparable to the numerical predictions and previous testing campaign results presented in Section 2.2. The same argument relating to the shaker type mentioned for the twin spar is valid when the identified data are compared with the testing campaign in [3]. Despite the similar geometry to the twin spar, the identified natural frequencies are higher. The main cause of this discrepancy is to be attributed to the more robust bridge used in the latter, and to its deformed shape. Additionally, the effect of the different input scenario is different on the main spar. The first and second modes show, in Figure 15 and Table 9, slight hardening behaviour and more pronounced softening behaviour on the third mode. Once again, the change in ω_{1-3} is not reflected in ζ_{1-3} and $\boldsymbol{\phi}_{1-2}$; for the former, the input scenario seems uncorrelated, while for the latter, it has no influence. Even so, for the medium-input scenario, a slight difference is noticed, but the difference itself does not create variance in the overall shape, but the

amplitude only. As already seen in the twin spar, $\boldsymbol{\phi}_3$ deviates from the trajectory of the same mode shape for lower amplitudes in positions 1R, 1L, 2L and 2R.

4.3. Spar and Tube

A numerical prediction for the spar and tube case was not performed in Section 2.2, but results similar to the main spar were expected and, indeed, obtained. For the first time in this work, a coupled mode—the third reported—is identified. This is most likely due to the effect of the tube on the dynamics of the structure and elastic axis position. As clearly shown in Figure 18, the mode in question is coupled between bending and torsion. However, that mode is the fourth overall mode of the specimen, as a mode is also present between 50 and 60 Hz, but it was disregarded as its displacement was dominated by the horizontal component. For this case, the influence of the input amplitude is not evident, but for the third mode, the softening behaviour can be identified from Table 8 and Figure 11. Once again, ζ_{1-3} seems to be unrelated to the input amplitude and $\boldsymbol{\phi}_{1-3}$ to remain constant.

4.4. Full Wing

As for the spar and tube, a prediction was not available in Section 2.2. The full-wing modal survey detected the first three vertically dominant modes, as it is clear in Figures 20 and 21 that there are four modes in the scrutinised interval, but only the first and the last two were found to be vertically dominant. For this case, the relationship between the input amplitude and the modes is unambiguous. In fact, all the modes show a clear softening behaviour. The identified ω_n decrease is clearly inverse to the input amplitude. This is a clear indication of some sort of breathing crack phenomenon somewhere in the wing's span [44], or, as pointed out in [45], it can depend on the asymmetry of the loading, which induces a twist moment, since the exciting force may not be applied in the shear centre. However, without further localised testing or inspections, this is not as certain, and its characterisation is left to future works. Even in this case, no relation was found between the change in ζ_{1-3} and the input amplitude, while the $\boldsymbol{\phi}_{1-3}$ remain constant for all cases.

4.5. Overall Considerations

It is possible, and beneficial, to compare the result of the analyses across all specimens to develop a greater understanding of the structures themselves.

The first mode, for all specimens and cases, is always found to be a true bending mode. The second and third mode for the two spars are also considered bending modes. However, these change with the spar and tube, where the third mode is now coupled with bending and torsion. In the full-wing case, only the first mode is still pure bending. Considering the first mode, it can be seen that the addition of the stiffening tube and of the skin changes the structure. When the tube is added, ω_1 increases, while with the further addition of the skin, ω_1 decreases. The tube effectively stiffens the structure, while the skin, designed to only transfer and not carry any loads [3], effectively can be seen as added mass on the structure. A comparison of the different structures based on ζ_n is not possible, as its changes do not follow any pattern, probably due to its intrinsic nature [46]. Concerning $\boldsymbol{\phi}_n$, it can be seen that $\boldsymbol{\phi}_1$ stays consistent throughout all specimens. This does not hold for $\boldsymbol{\phi}_2$, where differences can be assessed graphically (Figures 10, 14 and 18), particularly in channels #1–2LR, between the spars and the spar and tube assembly. The global considerations, focusing on the first mode, are that the different specimens behaved as expected, showing stiffening for the addition of the stiffening tube and, later, a decrease, when compared to the spar and tube, in stiffness for the full-wing scenario.

5. Conclusions

The high-aspect-ratio wing, its sub-assembly and parts, totalling four specimens, are verified via Ground Vibration Testing on a shaker table by the means of random vibration at three different amplitudes. The signals recorded from the experiments are used to

retrieve the modal parameters of the structures via the Least Squares Complex Exponential. Only the modal parameters of the first three modes dominated by vertical displacement are obtained, due to equipment constraints which allow only the recording of vertical accelerations for all nodes. The modal parameters, and the near-resonance regions of the Frequency Response Functions, are then used for non-linearity detection. Finally, the experimental data are shared with the scientific community in an open repository, linked in the Data Availability Statement. Non-linearities, in the form of softening, are detected for the full-wing case. Additionally, the modal results of the different specimens are compared, assessing that the addition of the stiffening tube raises the bending stiffness and that the further addition of the skin increases the structure's mass, reducing the corresponding resonance frequency. This work serves as the first extensive modal survey carried out on the flexible wing under scrutiny and tuning of the numerical predictions' Finite Element Model, using the modal data from this study, remains an objective of future work.

Author Contributions: Conceptualization, G.D., L.Z.F. and A.P.; methodology, G.D., L.Z.F. and A.P.; software, L.Z and G.D.; validation, G.D.; formal analysis, G.D.; investigation, G.D.; resources, D.I.I., J.F.W. and L.Z.F.; data curation, G.D.; writing—original draft preparation, G.D.; writing—review and editing, G.D., D.I.I., J.F.W., L.Z.F., and A.P.; visualisation, G.D.; supervision, D.I.I., J.F.W. and L.Z.F.; funding acquisition, L.Z.F. All authors have read and agreed to the published version of the manuscript.

Funding: The authors from Cranfield University disclosed receipt of the following financial support for the research, authorship and/or publication of this article: This work was supported by the Engineering and Physical Sciences Research Council (EPSRC) [grant number 2277626].

Institutional Review Board Statement: Not applicable.

Informed Consent Statement: Not applicable.

Data Availability Statement: Data available in a publicly accessible repository. The data presented in this study are openly available in the Cranfield Online Research Data (CORD) at https://doi.org/10.17862/cranfield.rd.19077023 (accessed on 20 June 2022) reference number 19077023.

Acknowledgments: The authors would like to thank Ivan Petrunin from the Centre for Autonomous and Cyber-Physical Systems at Cranfield University for providing the facilities and part of the equipment used for the tests.

Conflicts of Interest: The authors declare no conflict of interest. The funders had no role in the design of the study; in the collection, analyses or interpretation of data; in the writing of the manuscript or in the decision to publish the results.

Appendix A. Identification Data

Table A1. Twin spar: identified modal parameters.

	Low Input			Medium Input			High Input		
Mode	**1st**	**2nd**	**3rd**	**1st**	**2nd**	**3rd**	**1st**	**2nd**	**3rd**
ω_n	4.731	24.733	75.939	4.742	25.029	75.124	4.738	25.087	75.106
ζ_n	0.013	0.010	0.017	0.027	0.021	0.021	0.029	0.016	0.022
$\boldsymbol{\phi}_n$(1R)	0.137	0.531	0.626	0.138	0.525	0.580	0.149	0.550	0.268
$\boldsymbol{\phi}_n$(1L)	0.131	0.497	0.614	0.132	0.521	0.624	0.141	0.553	0.267
$\boldsymbol{\phi}_n$(2R)	0.303	0.744	0.056	0.303	0.746	0.074	0.309	0.809	0.069
$\boldsymbol{\phi}_n$(2L)	0.303	0.706	0.111	0.300	0.743	0.098	0.306	0.806	0.069
$\boldsymbol{\phi}_n$(3R)	0.662	0.152	−0.765	0.664	0.142	−0.693	0.664	0.123	−0.449
$\boldsymbol{\phi}_n$(3L)	0.640	0.117	−0.649	0.642	0.137	−0.656	0.669	0.126	−0.423
$\boldsymbol{\phi}_n$(4R)	0.995	−0.967	0.911	0.996	−0.997	0.977	0.9986	−1	0.965
$\boldsymbol{\phi}_n$(4L)	1	−1	1	1	−1	1	1	−0.997	1

Table A2. Main spar: identified modal parameters.

	Low Input			Medium Input			High Input		
Mode	**1st**	**2nd**	**3rd**	**1st**	**2nd**	**3rd**	**1st**	**2nd**	**3rd**
ω_n	4.855	26.966	76.851	4.866	27.050	76.195	4.876	27.057	75.805
ζ_n	0.033	0.010	0.014	0.029	0.016	0.020	0.029	0.014	0.022
$\boldsymbol{\phi}_n(1\mathrm{R})$	0.159	0.484	0.650	0.157	0.481	0.607	0.126	0.442	0.784
$\boldsymbol{\phi}_n(1\mathrm{L})$	0.171	0.500	0.708	0.160	0.487	0.641	0.116	0.435	0.918
$\boldsymbol{\phi}_n(2\mathrm{R})$	0.317	0.639	0.028	0.325	0.637	0.025	0.297	0.587	0.397
$\boldsymbol{\phi}_n(2\mathrm{L})$	0.302	0.680	0.104	0.306	0.656	0.071	0.277	0.603	0.438
$\boldsymbol{\phi}_n(3\mathrm{R})$	0.660	0.131	−0.755	0.679	0.133	−0.722	0.728	0.148	−0.834
$\boldsymbol{\phi}_n(3\mathrm{L})$	0.646	0.156	−0.656	0.663	0.144	−0.686	0.702	0.153	−0.749
$\boldsymbol{\phi}_n(4\mathrm{R})$	1	−1	0.942	1	−1	0.999	1	−1	0.951
$\boldsymbol{\phi}_n(4\mathrm{L})$	0.999	−0.977	1	0.999	−0.988	1	0.995	−0.992	1

Table A3. Spar and tube: identified modal parameters.

	Low Input			Medium Input			High Input		
Mode	**1st**	**2nd**	**3rd**	**1st**	**2nd**	**3rd**	**1st**	**2nd**	**3rd**
ω_n	5.252	25.933	76.242	5.151	25.958	75.770	5.163	25.941	75.135
ζ_n	0.022	0.014	0.017	0.030	0.011	0.034	0.036	0.010	0.034
$\boldsymbol{\phi}_n(1\mathrm{R})$	0.165	0.486	0.337	0.161	0.494	0.286	0.163	0.494	0.515
$\boldsymbol{\phi}_n(1\mathrm{L})$	0.158	0.439	0.658	0.153	0.441	0.595	0.156	0.440	0.798
$\boldsymbol{\phi}_n(2\mathrm{R})$	0.323	0.621	−0.185	0.318	0.631	−0.205	0.322	0.630	−0.173
$\boldsymbol{\phi}_n(2\mathrm{L})$	0.307	0.584	0.199	0.301	0.587	0.257	0.306	0.585	0.232
$\boldsymbol{\phi}_n(3\mathrm{R})$	0.672	0.107	−0.849	0.662	0.116	−0.823	0.672	0.112	−0.918
$\boldsymbol{\phi}_n(3\mathrm{L})$	0.646	0.0645	−0.320	0.663	0.072	−0.322	0.655	−0.068	−0.460
$\boldsymbol{\phi}_n(4\mathrm{R})$	1	−0.975	0.576	0.997	−0.967	0.595	0.999	−0.967	0.647
$\boldsymbol{\phi}_n(4\mathrm{L})$	0.999	−1	1	1	−1	1	1	−1	1

Table A4. Full wing: identified modal parameters.

	Low Input			Medium Input			High Input		
Mode	**1st**	**2nd**	**3rd**	**1st**	**2nd**	**3rd**	**1st**	**2nd**	**3rd**
ω_n	3.187	11.752	17.447	3.164	11.267	17.070	3.139	11.196	16.988
ζ_n	0.024	0.047	0.037	0.018	0.060	0.041	0.018	0.065	0.042
$\boldsymbol{\phi}_n(1\mathrm{R})$	0.187	1	0.090	0.187	1	0.089	0.192	1	0.086
$\boldsymbol{\phi}_n(1\mathrm{L})$	0.168	0.047	−0.474	0.174	0.047	−0.454	0.180	0.049	−0.420
$\boldsymbol{\phi}_n(2\mathrm{R})$	0.328	0.879	−0.204	0.329	0.895	−0.234	0.338	0.892	−0.241
$\boldsymbol{\phi}_n(2\mathrm{L})$	0.289	0.040	−0.682	0.278	0.041	−0.636	0.285	0.033	−0.572
$\boldsymbol{\phi}_n(3\mathrm{R})$	0.673	0.409	0.181	0.674	0.407	0.185	0.626	−0.204	−0.217
$\boldsymbol{\phi}_n(3\mathrm{L})$	0.624	−0.172	−0.288	0.620	−0.179	−0.250	0.655	−0.068	−0.460
$\boldsymbol{\phi}_n(4\mathrm{R})$	1	−0.195	1	1	−0.189	1	1	−0.297	1
$\boldsymbol{\phi}_n(4\mathrm{L})$	0.981	−0.640	0.610	0.986	−0.639	0.642	0.988	−0.712	0.663

References

1. Civera, M.; Zanotti Fragonara, L.; Surace, C. Using video processing for the full-field identification of backbone curves in case of large vibrations. *Sensors* **2019**, *19*, 2345. [CrossRef] [PubMed]
2. Pontillo, A.; Hayes, D.; Dussart, G.X.; Lopez Matos, G.E.; Carrizales, M.A.; Yusuf, S.Y.; Lone, M.M. Flexible high aspect ratio wing: low cost experimental model and computational framework. In Proceedings of the 2018 AIAA Atmospheric Flight Mechanics Conference, Kissimmee, FL, USA, 8–12 January 2018; American Institute of Aeronautics and Astronautics: Reston, VA, USA, 2018; pp. 1–15. [CrossRef]
3. Yusuf, S.Y.; Pontillo, A.; Weber, S.; Hayes, D.; Lone, M. Aeroelastic scaling for flexible high aspect ratio wings. In Proceedings of the AIAA Scitech 2019 Forum, San Diego, CA, USA, 3–7 January 2019; American Institute of Aeronautics and Astronautics: Reston, VA, USA, 2019; pp. 1–14. [CrossRef]
4. Hayes, D.; Pontillo, A.; Yusuf, S.Y.; Lone, M.M.; Whidborne, J. High aspect ratio wing design using the minimum energy destruction principle. In Proceedings of the AIAA Scitech 2019 Forum, San Francisco, CA, USA, 3–7 January 2019; American Institute of Aeronautics and Astronautics: Reston, VA, USA, 2019. [CrossRef]

5. Pontillo, A. High Aspect Ratio Wings on Commercial Aircraft: A Numerical and Experimental Approach. Ph.D. Thesis, Cranfield University, Cranfield, UK, 2020.
6. Spitznogle, F.R.; Quazi, A.H. Representation and analysis of time-limited signals using a Complex Exponential algorithm. *J. Acoust. Soc. Am.* **1970**, *47*, 1150–1155. [CrossRef]
7. Spitznogle, F.R.; Barrett, J.M.; Black, C.I.; Ellis, T.W.; LaFuze, W.L. *Representation and Analysis of Sonar Signals. Volume I. Improvements in the Complex Exponential Signal Analysis Computational Algorithm*; Technical Report; Office of Naval Research-Contract No. NOOO14-69-C0315; Defense Technical Information Center: Fort Belvoir, VA, USA, 1971.
8. Verhulst, T.; Judt, D.; Lawson, C.; Chung, Y.; Al-Tayawe, O.; Ward, G. Review for State-of-the-Art Health Monitoring Technologies on Airframe Fuel Pumps. *Int. J. Progn. Health Manag.* **2022**, *13*, 1–20. [CrossRef]
9. Rizzo, P.; Enshaeian, A. Challenges in bridge health monitoring: A review. *Sensors* **2021**, *21*, 4336. [CrossRef] [PubMed]
10. Dessena, G.; Civera, M.; Zanotti Fragonara, L.; Ignatyev, D.I.; Whidborne, J.F. A Loewner-based system identification and structural health monitoring approach for mechanical systems. *Struct. Health Monit.* **2022**, *17*.
11. Civera, M.; Mugnaini, V.; Zanotti Fragonara, L. Machine learning-based automatic operational modal analysis: A structural health monitoring application to masonry arch bridges. *Struct. Control. Health Monit.* **2022**, e3028. [CrossRef]
12. Dessena, G.; Ignatyev, D.I.; Whidborne, J.F.; Zanotti Fragonara, L. A Kriging Approach to Model Updating for Damage Detection. In Proceedings of the EWSHM 2022, Palermo, Italy, 4–7 July 2022; Rizzo, P., Milazzo, A., Eds.; Springer: Cham, Switzerland, 2022; Chapter 26; pp. 245–255. [CrossRef]
13. De Florio, F. *Airworthiness*; Elsevier: Amsterdam, The Netherlands, 2011. [CrossRef]
14. Keane, A.J.; Sóbester, A.; Scanlan, J.P. *Small Unmanned Fixed-Wing Aircraft Design*; John Wiley & Sons: Chichester, UK, 2017. [CrossRef]
15. Nöel, J.P.; Renson, L.; Kerschen, G.; Peeters, B.; Manzato, S.; Debille, J. Nonlinear dynamic analysis of an F-16 aircraft using GVT data. In Proceedings of the IFASD 2013—International Forum on Aeroelasticity and Structural Dynamics, Bristol, UK, 24–26 June 2013; pp. 1–13.
16. Lubrina, P.; Giclais, S.; Stephan, C.; Boeswald, M.; Govers, Y.; Botargues, N. AIRBUS A350 XWB GVT: State-of-the-Art Techniques to Perform a Faster and Better GVT Campaign. In *Topics in Modal Analysis II, Volume 8*; Allemang, R., Ed.; Conference Proceedings of the Society for Experimental Mechanics Series; Springer: Cham, Switzerland, 2014; Volume 45, pp. 243–256. [CrossRef]
17. Lemler, K.J.; Semke, W.H. Application of modal testing and analysis techniques on a sUAV. In *Special Topics in Structural Dynamics*; Springer: New York, NY, USA, 2013; Volume 6, pp. 47–57. [CrossRef]
18. Weber, S.; Kissinger, T.; Chehura, E.; Staines, S.; Barrington, J.; Mullaney, K.; Fragonara, L.Z.; Petrunin, I.; James, S.; Lone, M.; et al. Application of fibre optic sensing systems to measure rotor blade structural dynamics. *Mech. Syst. Signal Process.* **2021**, *158*, 107758. [CrossRef]
19. Göge, D. Automatic updating of large aircraft models using experimental data from ground vibration testing. *Aerosp. Sci. Technol.* **2003**, *7*, 33–45. [CrossRef]
20. Zhang, W.; Lv, Z.; Diwu, Q.; Zhong, H. A flutter prediction method with low cost and low risk from test data. *Aerosp. Sci. Technol.* **2019**, *86*, 542–557. [CrossRef]
21. Pecora, R.; Amoroso, F.; Palumbo, R.; Arena, M.; Amendola, G.; Dimino, I. Preliminary aeroelastic assessment of a large aeroplane equipped with a camber-morphing aileron. In Proceedings of the Industrial and Commercial Applications of Smart Structures Technologies, Portland, OR, USA, 26–27 March 2017; Clingman, D.J., Ed.; SPIE: Bellingham, WA, USA, 2017; Volume 10166, p. 101660. [CrossRef]
22. Dessena, G.; Civera, M.; Pontillo, A.; Ignatyev, D.I.; Whidborne, J.F.; Zanotti Fragonara, L. Comparative Study on Novel Modal Parameters Extraction Methods for Aeronautical Structures. *in preparation*.
23. Mugnaini, V.; Zanotti Fragonara, L.; Civera, M. A machine learning approach for automatic operational modal analysis. *Mech. Syst. Signal Process.* **2022**, *170*, 108813. [CrossRef]
24. Tsatsas, I.; Pontillo, A.; Lone, M. Aeroelastic damping estimation for a flexible high-aspect-ratio wing. *J. Aerosp. Eng.* **2022**, *35*, 1–27. [CrossRef]
25. Noviello, M.C.; Dimino, I.; Concilio, A.; Amoroso, F.; Pecora, R. Aeroelastic Assessments and Functional Hazard Analysis of a Regional Aircraft Equipped with Morphing Winglets. *Aerospace* **2019**, *6*, 104. [CrossRef]
26. Ewins, D.J. *Modal Testing Theory, Practice and Application*, 2nd ed.; Research Studies Press: Baldock, UK, 2000; p. 562.
27. Worden, K.; Tomlinson, G.R. *Nonlinearity in Structural Dynamics Detection, Identification and Modelling*; Institute of Physics Publishing: Bristol, UK, 2001.
28. Kerschen, G.; Worden, K.; Vakakis, A.F.; Golinval, J.C. Past, present and future of nonlinear system identification in structural dynamics. *Mech. Syst. Signal Process.* **2006**, *20*, 505–592. [CrossRef]
29. Dossogne, T.; Noël, J.P.; Grappasonni, C.; Kerschen, G.; Peeters, B.; Debille, J.; Vaes, M.; Schoukens, J. Nonlinear ground vibration identification of an F-16 aircraft—Part II: Understanding nonlinear behaviour in aerospace structures using sine-sweep testing. In Proceedings of the International Forum on Aeroelasticity and Structural Dynamics, IFASD 2015, Saint Petersburg, Russia, 28 June–2 July 2015; pp. 1–19.
30. Kerschen, G.; Soula, L.; Vergniaud, J.B.; Newerla, A. Assessment of Nonlinear System Identification Methods using the SmallSat Spacecraft Structure. In *Advanced Aerospace Applications, Volume 1*; Proceedings of the Society for Experimental Mechanics Series; Springer: Berlin/Heidelberg, Germany, 2011; Volume 1, pp. 203–219. [CrossRef]

31. Noël, J.; Kerschen, G. Nonlinear system identification in structural dynamics: 10 more years of progress. *Mech. Syst. Signal Process.* **2017**, *83*, 2–35. [CrossRef]
32. Civera, M.; Grivet-Talocia, S.; Surace, C.; Zanotti Fragonara, L. A generalised power-law formulation for the modelling of damping and stiffness nonlinearities. *Mech. Syst. Signal Process.* **2021**, *153*, 107531. [CrossRef]
33. Kerschen, G.; Peeters, M.; Golinval, J.C.; Stéphan, C. Nonlinear modal analysis of a full-scale aircraft. *J. Aircr.* **2013**, *50*, 1409–1419. [CrossRef]
34. Zanotti Fragonara, L.; Boscato, G.; Ceravolo, R.; Russo, S.; Ientile, S.; Pecorelli, M.L.; Quattrone, A. Dynamic investigation on the Mirandola bell tower in post-earthquake scenarios. *Bull. Earthq. Eng.* **2017**, *15*, 313–337. [CrossRef]
35. Dezi, F.; Gara, F.; Roia, D. Dynamic Characterization of Open-ended Pipe Piles in Marine Environment. In *Applied Studies of Coastal and Marine Environments*; InTechOpen: London, UK, 2016; pp. 169–204. [CrossRef]
36. Brown, D.L.; Allemang, R.J.; Zimmerman, R.; Mergeay, M. Parameter estimation techniques for modal analysis. *SAE Trans.* **1979**, *88*, 790003–790266. [CrossRef]
37. Maia, N.M.M. Extraction of Valid Modal Properties from Measured Data in Structural Vibrations. Ph.D. Thesis, Imperial College London: London, UK, 1988.
38. Stratasys. Digital ABS Plus. 2021. Available online: https://www.stratasys.com/en/materials/materials-catalog/polyjet-materials/digital-abs-plus/ (accessed on 26 June 2021).
39. Stratasys. Agilus 30. 2021. Available online: https://www.stratasys.com/en/materials/materials-catalog/polyjet-materials/agilus30/ (accessed on 26 June 2021).
40. Blevins, R.D. *Formulas for Dynamics, Acoustics and Vibration*; John Wiley & Sons: Hoboken, NJ, USA, 2015; pp. 1–448. [CrossRef]
41. Hu, X. Effects of Stinger Axial Dynamics and Mass Compensation Methods on Experimental Modal Analysis. Ph.D. Thesis, Iowa State University, Ames, IA, USA, 1992. [CrossRef]
42. Schulze, A.; Zierath, J.; Rosenow, S.E.; Bockhahn, R.; Rachholz, R.; Woernle, C. Optimal sensor placement for modal testing on wind turbines. *J. Phys. Conf. Ser.* **2016**, *753*, 72031. [CrossRef]
43. Dessena, G. *Dataset: Ground Vibration Testing of a Flexible Wing: A Benchmark and Case Study*; Cranfield University: Cranfield, UK, 2022.
44. Yang, L.; Mao, Z.; Wu, S.; Chen, X.; Yan, R. Nonlinear dynamic behavior of rotating blade with breathing crack. *Front. Mech. Eng.* **2021**, *16*, 196–220. [CrossRef]
45. Pagani, A.; Carrera, E. Unified formulation of geometrically nonlinear refined beam theories. *Mech. Adv. Mater. Struct.* **2018**, *25*, 15–31. [CrossRef]
46. Civera, M.; Calamai, G.; Zanotti Fragonara, L. System identification via Fast Relaxed Vector Fitting for the Structural Health Monitoring of masonry bridges. *Structures* **2021**, *30*, 277–293. [CrossRef]